



Modeling sediment transport patterns during an upwelling event

K. Huhn,¹ A. Paul,¹ and M. Seyferth¹

Received 17 June 2005; revised 10 April 2007; accepted 26 April 2007; published 4 October 2007.

[1] Being one of the most outstanding hydrodynamic processes at ocean margins, upwelling is not only a key factor controlling bioproduction but also acts as a driving mechanism for sediment transport. In order to quantify its capability to erode and transport sedimentary particles without being masked by other oceanographic processes, we present a numerical model only forced by surface wind drag. Thereby, transport of particles is not only controlled by upwelling circulation, but also by their physical properties as well as time and location of release into the water column. The study combines a hydrodynamic finite difference model and Lagrangian particle tracing technique. Model geometry mimics a two-dimensional profile from the passive margin offshore Walvis Bay, Namibia. Model runs describe a 5-day wind-forcing event and a subsequent 20-day period of relaxation. As our work is also motivated by paleoceanographic questions, a lowered sea level geometry is used simulating Last Glacial Maximum (LGM) conditions. Results suggest the establishment of a long-lasting circulation comprising an offshore-directed surface layer and an onshore-directed bottom current. Shelf currents are vigorous but short-lasting, allowing transport of particles up to sand size. In contrast, transport at the upper slope is more persistent but restricted to smaller grain sizes. Sea level changes cause a shift of upwelling front in cross-shelf direction and of sedimentary deposition centers along the slope. Transport paths of surface source tracers show systematic variations, which can be evaluated in terms of grain-size fractionation as well as temporal and spatial clusters.

Citation: Huhn, K., A. Paul, and M. Seyferth (2007), Modeling sediment transport patterns during an upwelling event, *J. Geophys. Res.*, 112, C10003, doi:10.1029/2005JC003107.

1. Introduction

[2] Coastal upwelling is a result of Ekman pumping in response to alongshore winds acting at the sea surface [e.g., Luther and O'Brien, 1985; Hay and Brock, 1992; Thurman and Trujillo, 1999]. The divergence or offshore transport of surface water away from the coastal boundary takes place within the surface boundary layer (SBL). Its replacement by water from central levels is completed by onshore currents within the lower part of the water column, especially the bottom boundary layer (BBL) [e.g., Thurman and Trujillo, 1999]. Coastal upwelling occurs mainly along the west coasts of continents controlled by the coast-parallel Trade Winds and the position of the Intertropical Convergence Zone [e.g., Shannon and O'Toole, 1999]. For example, the Benguela system is one of the major upwelling systems along the coastline of South Africa, Namibia, and Angola [e.g., Nelson and Hutchings, 1983; Shannon, 1985; Chapman and Shannon, 1985; Shannon and Nelson, 1996]. Oceanography of this region is in many respects similar to the Humboldt Current off Peru and Chile, the California Current of the west coast of the US and the

Canary Current off northwest Africa [Shannon and O'Toole, 1999].

[3] Upwelling regions are not only of ecological and economic interest because of high bioproduction rates due to the enrichment of nutrient-rich water, but they also leave their imprints on the sedimentary record. This enables the reconstruction of environmental conditions as well as climate changes through time [e.g., Hay and Brock, 1992]. In addition, upwelling currents can also trigger sediment transport processes also documented in the sedimentary signal. Hence upwelling cells are displaced in a seaward direction in response to sea level low-stands the Last Glacial Maximum which coevally causes a drastically increase of total mass accumulation of organic material on continental slope areas, for example, at the continental slope offshore Namibia [e.g., Mollenhauer et al., 2002]. Ideally, transport of mobile particles in a stationary upwelling cell can describe a loop embracing offshore transport in the SBL, gravitational sinking through the water column and onshore transport in the BBL [e.g., Chamley, 1990]. The location of the sediment source and the release time are important key parameters for sediment transport pattern. However, different redistribution processes of foraminifera and alkenones due to their actual shape and size causes a large age offset observed in sediment cores from the upper continental slope off Namibia [Mollenhauer et al., 2003]. Besides, different sediment types show typical sink, deposition and erosion

¹DFG Research Center Ocean Margins, Bremen, Germany.

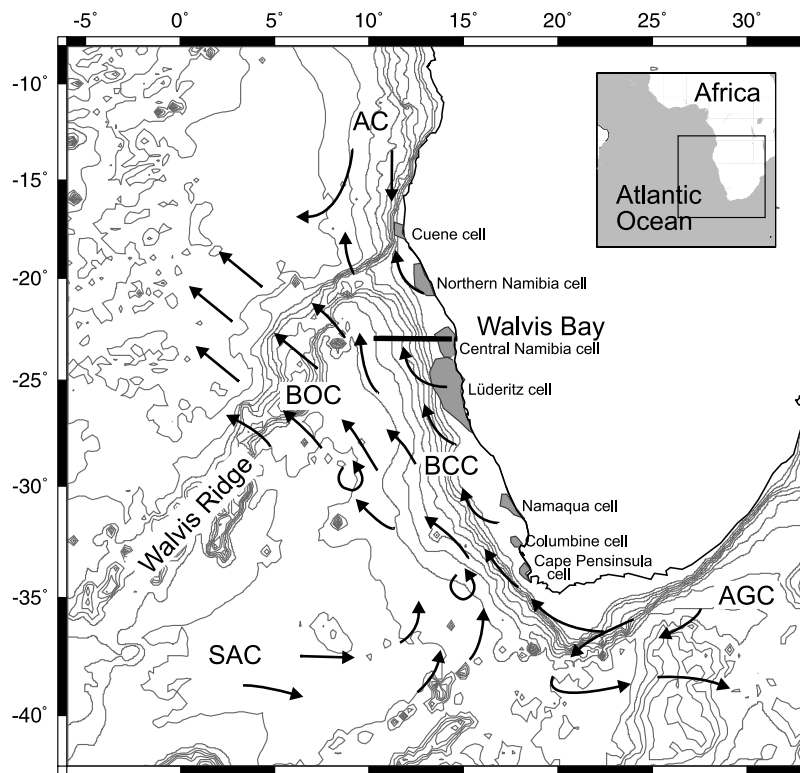


Figure 1. Sketch map of the passive margin offshore Namibia, showing the location of the M57/2 profile, large-scale bathymetry, the general pattern of surface currents (arrows: BCC, Benguela Coastal Current; BOC, Benguela Oceanic Current; SAC, South Atlantic Current; AGC, Agulhas current; AC, Angola Current), and the upwelling regions. Modified after *Wefer et al.* [1996], *Lutjeharms and Stockton* [1987], and *Shannon and Nelson* [1996].

behavior depending on their physical properties, for example, grain size, shape, and density [e.g., *Zanke*, 1982; *Allen*, 1985]. Therewith, the actual shape and extent of sedimentary transport pathways are controlled by the hydrodynamic environment, for example, current conditions, the sediment types as well as the margin geometry and/or sea level setting.

[4] However, up to now less is known about the transport pathways and redistribution processes of different sediment types during a coastal upwelling event. Additionally, the displacement of sediment deposition centers due to sea level changes is not fully understood. For this reason, our studies are motivated by paleoceanographic questions regarding the effect of sea level change during the Last Glacial Maximum (~19,000–23,000 years before present) as a better understanding of the sediment transport mechanisms in these regions would enable a more precise interpretation of the sedimentary records.

[5] Our studies focus on the temporal and spatial distribution of sediment transport patterns during coastal upwelling as a function of grain size, source location, and sediment injection time, as well as margin geometry or respectively sea level conditions. We simulate an idealized single upwelling event to exclusively evaluate its capabilities to drive and control the sediment transport. Furthermore, we used a 2D vertical cross section of a continental margin only focusing on wind stress induced currents while all other alongslope driving mechanisms are factored out. All these

simplifications enable parameter sensitivity studies to quantify influences of the above mentioned controlling factors for their potential of sediment transport of distinct particles within an upwelling cell. In that, we provide a first piece for the analysis of a complex puzzle of processes to gain a deeper insight into the sediment transport mechanisms in upwelling regions.

[6] Although the major aim of these studies is a parameter sensitivity analysis of sediment transport in upwelling regions in general, numerous information about margin geometry, wind-forcing, sediment budget, current velocities etc. are necessary to build a realistic model setup. Hence the models presented in this study have been inspired by the upwelling offshore Walvis Bay, Namibia, as part of the Benguela current system (Figure 1). Here the northward alongshore component of the southeast Trade Wind is the driving force for coastal upwelling processes (Figure 1) [e.g., *Peterson and Stramma*, 1991; *Shannon and Nelson*, 1996; *Wedepohl et al.*, 2000; *Christensen and Giraudeau*, 2002]. The mean speed of the Benguela Current has been estimated by *Shannon* [1985] to be 17 cm s^{-1} ; *Wedepohl et al.* [2000] propose variations from $<11 \text{ cm s}^{-1}$ to a maximum of 23 cm s^{-1} . The wind field, topographic features and orientation of the coast results in the formation of a number of upwelling cells, the Lüderitz cell (27°), northern Namibian, central Namibian (Walvis Bay), Namaqua, and Cape Peninsula (Figure 1) [*Shannon and O'Toole*, 1999]. Usually the Benguela upwelling occurs

during the whole year whereas the intensity shows annual and interannual changes according to the strength of the coast-parallel Trade Winds [Hagen *et al.*, 2001]. Thus strong upwelling occurs throughout the year at the Lüderitz cell [Stander, 1964] whereas the secondary upwelling cells are more sensitive to interannual variations [Hagen *et al.*, 2001]. In addition, hydrodynamic patterns are modified by the potential presence of a southward-directed undercurrent [Barange and Pillar, 1992; Giraudeau *et al.*, 2000], mesoscale eddies derived from the Agulhas current system [Garzoli *et al.*, 1996], as well as tidal forces, resulting in highly variable circulation patterns over time and space. Detailed description of the physical oceanography of the upwelling region off southwest Africa has been presented by Bang [1971] and more recently by Shannon and Nelson [1996], Lass *et al.* [2000], and Hagen *et al.* [2001].

[7] As detailed hydrographic data, which are essential as input for our ocean circulation model, are available from the several Meteor cruises to Walvis Bay [e.g., Zabel *et al.*, 2003], we adopt the margin geometry of a E-W-trending cross section along 23°S perpendicular to the slope. We simulate as single upwelling event caused by a wind stress anomaly typical for this region. However, as hydrodynamic conditions are very complex in this region as well as intensity and time of upwelling events changes significantly along the Namibian margin [Shannon and Nelson, 1996; Shannon and O'Toole, 1999; Hagen *et al.*, 2001], our simplified 2D model cannot serve as a true case study for the upwelling off Namibia. To enable this, at least an extension of our model into 3D would be essential.

[8] For these investigations, we combine for the first time a classical ocean circulation model ROMS (Regional Ocean Modelling System, Ocean Modeling Group at Rutgers University [e.g., Haidvogel *et al.*, 2000]) with a newly implemented particle tracing code in the commercial software FLAC (Fast Lagrangian Analysis of Continua; Itasca). The hydrodynamic ROMS model is used to calculate the water velocity field because on the basis of terrain-following coordinates it is capable to simulate circulation in a model domain spanning a large range of different water depths. Thus ROMS has been successfully applied to several oceanographic scenarios including wind-driven flow near submarine canyons [She and Klinck, 2000] and a large-scale model of the Benguela Current [Penven *et al.*, 2001].

[9] A mean to study the behavior of distinct particles is the application of modified Lagrangian tracers bearing the outlined physical properties [e.g., Haupt *et al.*, 1994]. Using this “offline” approach, displacement paths or respectively transport patterns of a numerous of different individual grains can be traced with less calculation time.

2. Model Setup

2.1. Hydrodynamic ROMS Model

[10] The Regional Ocean Modeling System (ROMS) has been coded by the Ocean Modeling Group at Rutgers University and the UC Los Angeles [e.g., Haidvogel *et al.*, 2000; Ezer *et al.*, 2002; Shchepetkin and McWilliams, 2004]. ROMS is a free-surface, hydrostatic, primitive equation ocean model that uses stretched, terrain-following coordinates in the vertical and orthogonal curvilinear

coordinates in the horizontal. It is derived from the earlier S-coordinate Rutgers University Model (SCRUM) described by Song and Haidvogel [1994]. Distinguishing between barotropic (fast) and baroclinic (slow) modes, a split-explicit time stepping scheme is used to solve the hydrostatic primitive equations for momentum. A finite number of barotropic time steps, within each baroclinic step, is carried out to evolve the free-surface and vertically integrated momentum equations. In the vertical, the primitive equations are discretized over variable topography using stretched terrain-following coordinates [Song and Haidvogel, 1994]. The stretched coordinates allow increased resolution in areas of interest, such as thermocline and BBL. Pressure gradient errors, arising owing to splitting of the pressure gradient term into an along-sigma component and a hydrostatic correction Haidvogel and Beckmann [1999] are reduced following Song and Wright [1998] and Shchepetkin and McWilliams [1998].

[11] In this study, the hydrodynamic model is designed to mimic an E-W-trending, vertical bathymetric profile located at 23°S offshore Walvis Bay ranging from 10.5 to 14.5°E. Here the passive margin formed a 130 km wide shelf which is characteristically subdivided into an inner and an outer shelf flat separated by a relatively steep ramp which we refer to as “inner shelf break” (Figure 2a). Corresponding bathymetric data taken from Smith and Sandwell [1997] indicate water depths around 150 m on the inner and up to 350 m on the outer shelf, respectively. The transition of the outer shelf to the continental slope which we term “outer shelf break” is characterized by a small bulge resulting in a synform shape of the outer shelf area. The character of surface sediments is highly variable both along the profile and perpendicular to it [Zabel *et al.*, 2003; Pufahl *et al.*, 1998]. However, a common and laterally consistent feature is the presence of a mud belt in the vicinity of the coast; additional depocenters have been found to occur at the uppermost slope and in the depression of the concave outer shelf [Bremner, 1983].

[12] Hence our model mirrors the geometry of an idealized continental margin (Figure 2a). Laterally the model grid extends over 408 km including the cold water belt of uplifted central water observed along the Walvis Bay upwelling cell [e.g., Hagen *et al.*, 2001]. To avoid disturbances of circulation by a closed vertical wall at the sea side of the models, a fictive sinusoidal western ocean margin has been added (Figure 2a). The model domain is periodic in the north-south direction to allow for coast-parallel transport of water masses; one grid cell is present in the out-of-plane direction, so that the model dimension is actually 2D. The model is discretized into 40 vertical levels with enhanced resolution of the SBL and BBL (see Figure 2a and Table 1). Grid spacing along the transect is 2 min, corresponding to a cell width of ~3.4 km and a number of 260 grid cells.

[13] Upwelling circulation is forced by north-directed wind drag perpendicular to the model plane. The setup is based on the wind-driven upwelling test case by the Rutgers IMCS Ocean Modeling Group (H. G. Arango, Wind-driven upwelling/downwelling over a periodic channel, ROMS source code, 2002, available at <http://marine.rutgers.edu>).

[14] During the METEOR cruise 48-2 cruise at least two strong wind events were observed, one of ~5, the other of ~3 days duration similar to other measurements [Shannon

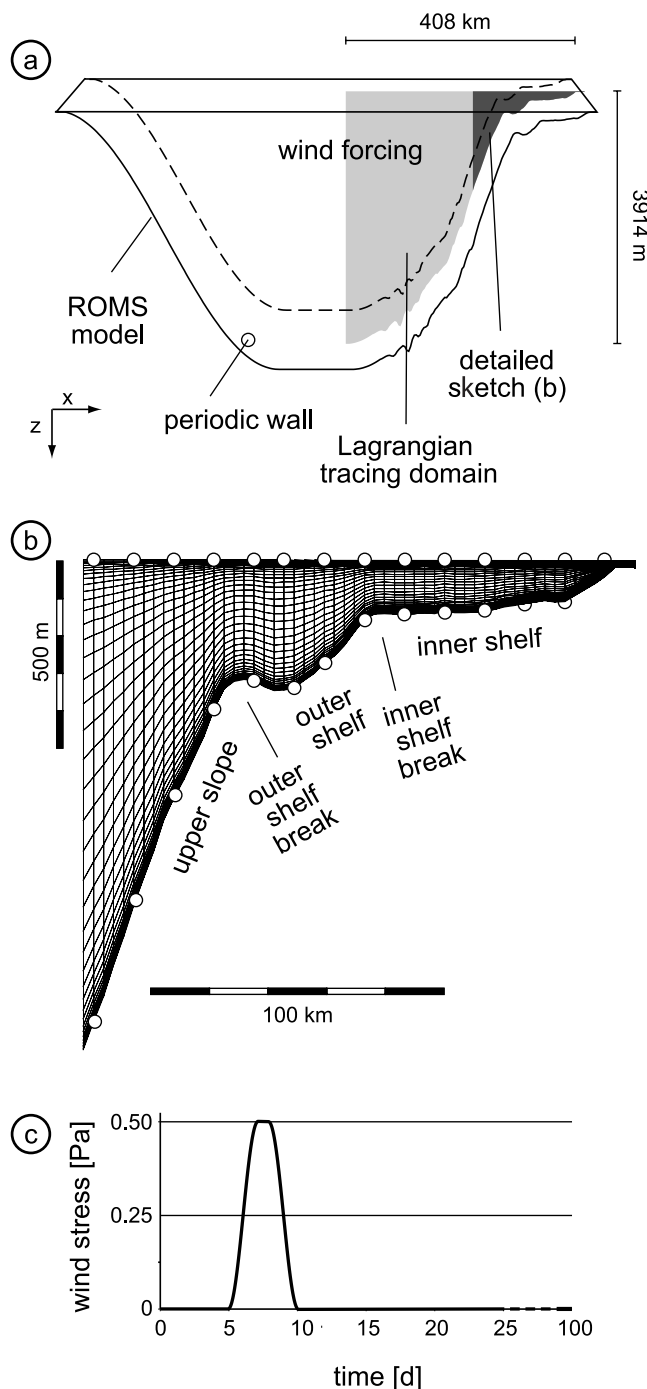


Figure 2. Model setup. (a) Hydrodynamic (ROMS) model embraces the model transect (i.e., the domain of particle tracing) marked in Figure 1, and a virtual ocean margin on the left; the model domain is divided into 260 grid cells along the horizontal and 40 cells along the vertical axis, respectively; two grid cells are present perpendicular to the transect. (b) Schematic detailed view to the proximal part of the transect showing grid cells, terminology, and sediment sources (circles). (c) Temporal evolution of wind-forcing applied to the model surface. The model runs cover a total time of 30 days. Wind stress up to 0.5 Pa is applied at the model surface for a time span of 5 days. After its cessation, the model runs for a further 20 days.

and Nelson, 1996]. Recorded wind velocities reach values of 14.4–17.5 m s⁻¹. The mean velocity value of 16 m s⁻¹ correlates with former data, for example, that of *Mohrholz et al.* [1999] which recorded maximum values of about 17 m s⁻¹ south of 16°S. We calculated the wind stress values using the standard formula $\tau = C_D \rho |\mathbf{W}| \mathbf{W}$, where τ is the wind stress vector, ρ is the density of air at 20°C (1.204 kg m⁻³), \mathbf{W} is the wind velocity adjusted to 10-m height and C_D the variable drag coefficient. The drag coefficient for a neutral atmosphere above the sea surface was chosen according to *Smith* [1988] with $C_D = 1.5E-03$. This supplies a mean wind stress of 0.47 N m⁻² or 0.47 Pa.

[15] In accordance to that, out-of-plane north-directed wind stress up to ~ 0.5 Pa or respectively 16 m s⁻¹ is applied to the model surface for a time span of five days (Figure 2c). This wind-forcing comprises a two day phase of sinusoidal intensification and decrease, respectively. After its cessation, the model runs for further 20 days (Figure 2c). The temperature and salinity stratification is initialized from the deepest Meteor M57/2 station [*Zabel et al.*, 2003]. During the whole model run, kinematic surface heat and freshwater fluxes are set to zero.

[16] Since the intention of the models is to isolate the effects of upwelling other oceanographic factors are not taken into account, for example, highly energetic waves and tides in shallow-water domains. However, although tides or waves induced by background wind conditions are capable to provide unidirectional transport mechanisms along the model traverse, their effects may be neglected on a large scale compared to that of upwelling circulation. Furthermore, the model does not take into account large-scale ocean currents. However, the effect of a coast-parallel surface current is limited, since its main velocity component is out of the model plane. In contrast, the presence of a poleward undercurrent could modify the model scenario in a more significant manner by providing a background velocity field differing from the static initial conditions assumed in the models. Consequent Ekman pumping would imply the presence of an offshore-directed background bottom current and the deeper parts of the water column might be permanently out of reach for wind-induced upwelling circulation.

[17] As we also want to investigate the sensitive of sediment transport pattern as a function of sea level conditions, a second model geometry with a sea level 130 m lower is settled up. Here parts of the inner shelf fell dry. Consequently, the present-day outer shelf acts as a narrow (<50 km) and relatively deep (200 m) shelf platform. Such a sea level stand reflects conditions which are postulated for the Last Glacial Maximum [e.g., *Wefer et al.*, 1996]. However, an interpretation as an upwelling event during the LGM is impossible because of the simplification of wind-forcing as well as the 2D approach. As aim of these simulations is to study the role of sea level or changes in margin geometry all other model characteristics kept constant.

2.2. Particle-Tracing FLAC Model

[18] Besides calculating the velocity field within the Eulerian grid of a hydrodynamic model, a common technique to follow up the fluids motion is the use of Lagrangian tracers, virtual massless “particles” advected by the fluid

Table 1. Units, Symbols, and Default Values Addressing Model Setup and Boundary Conditions

	Unit or Symbol	Default Value
<i>ROMS: Model Geometry, Discretization, and Boundary Conditions</i>		
Lateral model extent	m	385.4×10^3
Maximum water depth	m	3914.0
Number of grid points	-	10400
Calculation time step	s	300.0
Duration of model run	d	104.16
Linear bottom drag coefficient	m s^{-1}	3.0×10^{-4}
Initial surface temperature	$^{\circ}\text{C}$	18
Maximum wind-forcing	Pa	0.5
Duration of wind-forcing	d	5.0
<i>Particle Tracing Module: Model Geometry and Discretization</i>		
Lateral model extent	m	852.8×10^3
Coupling time step	s	21600.0
Calculation time step	s	60.0
<i>Particle Tracing Module: Tracers</i>		
Injected grain sizes	Φ	{3, 4, 5, 6, 7, 8}
Density	kg m^{-3}	2650.0
Shape factor FF	-	0.7

[e.g., *de Vries and Döös*, 2001]. In this study, we present an expansion of this technique using tracers characterized by the physical properties of sedimentary particles, for example, grain size, shape, and density. These Lagrangian calculations are carried out on the basis of the ROMS velocity fields in an “offline” manner with the commercial code FLAC.

[19] Figure 2b illustrates the particle tracing domain, showing the model grid, its refinement toward the SBL and BBL and the distribution of sediment sources. In contrast to the hydrodynamic models only the eastern part of the model domain is taken into account. In addition, horizontal particle motion is calculated in the x axis or cross-shelf direction respectively whereas particle settling or resuspension behavior is separately accounted in the vertical z -direction. This is appropriate, since the calculation of critical deposition and resuspension velocities takes into account the 3D velocity field. Hence all transport paths presented in this study have to be interpreted as projections of the actual path onto the xz -model plane; similarly, the computed transport distances have to be understood as the component parallel to the model section.

[20] We adopt ROMS velocities in a time interval of 6 hours to calculate sediment dynamics with FLAC. Therefore cross-shelf and vertical velocities from ROMS are applied to the respective grid points of the FLAC model. As the FLAC software expects densely sampled velocity information to achieve continuous and stable particle transport trough time, a linear interpolation of the ROMS velocities is performed. Hence within the FLAC simulations we used a time interval of 60 s. In the BBL cells, the particle transport is estimated by comparison of calculated horizontal and vertical bottom velocity values versus critical velocities defined by the physical properties of tracers and their interaction with the fluid. Therefore the explicit horizontal drag and settling terms are implemented within the velocity calculation. FLAC provides information if a tracer is deposited, transported or eroded at each time step along the seafloor. Similarly, sinking behavior is simulated also using horizontal and vertical velocities for the different tracer

types. However, vertical ROMS velocities affected only smaller particles (see section 3.3) and they are negligibly small compared to sinking velocities for larger tracers (Figure 3). Particle interactions in the water column and in suspension in the BBL as well as particle flocculation are not taken into account because this would go beyond the scope of this parameter sensitivity study [e.g., *Khalili et al.*, 2001; *Goharzadeh et al.*, 2005].

[21] The final output of FLAC comprises information about particle distribution in the BBL and the water column at each time step. On the basis of the history of tracer positions, particle pathways can be displayed as function of release time (e.g., before, during, or after the upwelling event), source position (e.g., at the sea level, at the seafloor), and particle shape (e.g., particle sizes).

[22] Gravitational settling through the water column is traditionally described by Stoke’s law [e.g., *Allen*, 1985; *Middleton and Southard*, 1984]. A more elaborate formula by *Zanke* [1982] results in very similar sinking velocities to those predicted by Stoke. In contrast to numerous other mathematical approaches which were developed for specific environments and case studies [e.g., *Gibbs*, 1985; *Hsü*, 1989; *McCave and Gross*, 1991], this equation enables the description of the settling behavior of a large grain spectra under different current conditions. Thus it describes the settling behavior similar to Stoke’s for low Reynold’s numbers whereas it is similar to the Newton approach for large Reynold’s numbers. These are necessary requirements not covered by other approaches. A detailed discussion on different approaches to describe settling velocities is given by *Haupt* [1995]. Furthermore, sediment transport along the BBL and in suspension is implemented into this formula as well as it enables investigation of sediment type and grain shape respectively. Hence the relationship by *Zanke* [1982],

$$\bar{v}_s = \frac{12\nu}{d(2.7 - 2.3FF)} \cdot \left(\sqrt{1 + \left(0.21 \cdot d \cdot \left(\frac{(\rho_s - \rho_f) \bar{g}}{\nu^2 \rho_f} \right)^{\frac{1}{3}} \right)^2} (2.7 - 2.3FF) - 1 \right), \quad (1)$$

takes into account the particle diameter d , the kinematic viscosity of the fluid ν , gravity \bar{g} , and the densities of the particle ρ_s and the fluid ρ_f , respectively. Additionally it comprises a shape factor FF

$$FF = \frac{d_s}{\sqrt{d_i d_i}} \quad (2)$$

based on the largest, intermediate, and shortest grain diameters (d_i , d_i , and d_s) which amounts to 1 for spherical particles and to 0.7 for natural grains where $d_i * d_i = 2 d_s$ applies; a uniform value of 0.7 has been applied in this study which was successfully used to simulate the sediment transport pattern for example in the Northern Atlantic [*Seidov and Haupt*, 1995]. The resulting sinking velocity components are added to the horizontal and vertical velocity field determined by the ROMS calculations.

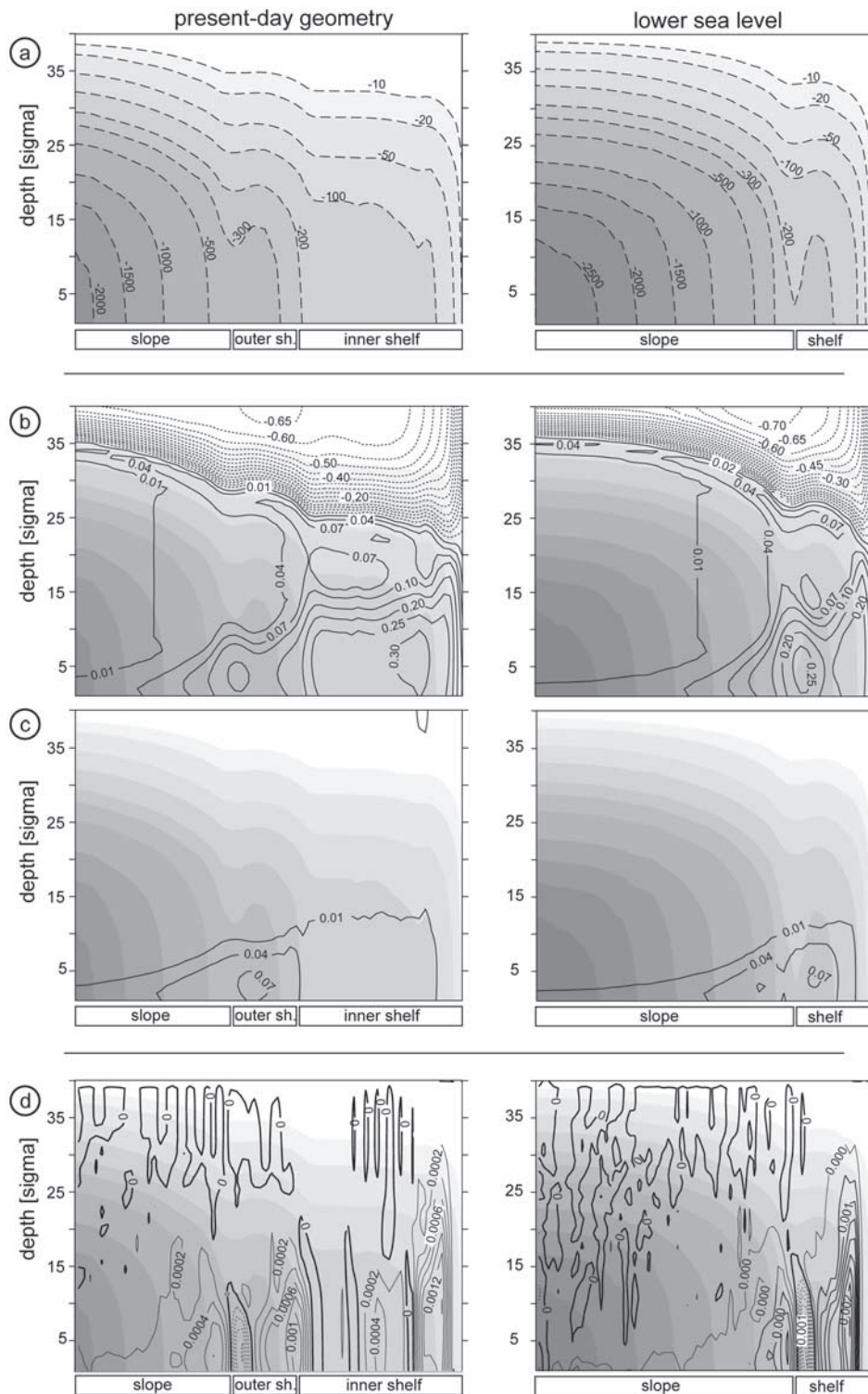


Figure 3. (a) ROMS results are plotted using a stretched sigma-coordinate system; for comparison, absolute water depth (meters) is indicated by shaded contours, which are also visible in the subsequent plots. (b) Horizontal velocities at the end of wind-forcing (day 10 from the beginning of the model run); positive values are directed onshore, i.e., to the right; negative velocity contours are dashed. (c) Horizontal velocities 20 days after cessation of wind-forcing (day 30); the locus of maximum onshore velocities moves from the shelf to the uppermost part of the slope. (d) Vertical velocities at the end of wind-forcing; maximal velocity can be observed along steeper parts of the continental margin.

Table 2. Grain Sizes of Tracers Used in the Model

Description	Grain Size, mm	Grain Size, Φ	Analytical Sinking Distance, m/100 days
Fine-grained sand	0.125	3	3.5×10^5
Sand/silt	0.0625	4	1.5×10^5
Coarse-grained silt	0.0312	5	5.1×10^4
Medium-grained silt	0.0156	6	1.4×10^4
Fine-grained silt	0.00781	7	3.4×10^3
Silt/clay	0.00391	8	8.6×10^2

[23] Transport of particles in the BBL is controlled by critical velocities describing the onset of transport (i.e., erosion of a previously deposited particle) and deposition. The actual transport velocity is computed on the basis of the bottom-parallel velocity and the sinking velocity of the individual particle. In detail, we have employed a critical (minimum) velocity describing the onset of bottom transport

$$\bar{v}_{bottom} = 2.8 \left(\left(\frac{\rho_s - \rho_f}{\rho_f} \right) \bar{g} d \right)^{0.5} + 14.7 \frac{v}{d} c \quad \text{with } c = 1, \quad (3)$$

a critical (minimum) velocity describing the onset of suspension transport $\bar{v}_{susp} = 8.4 \bar{v}_s$, and a critical (maximum) velocity for particle deposition $\bar{v}_{dep} = 3.93 \bar{v}_s$ [Zanke, 1982].

[24] In order to evaluate the transport capabilities for a large span of particle sizes potentially present in the ocean, monitored particle diameters range from 3 Φ (fine sand) to 8 Φ (silt/clay transition) according to the logarithmic Wentworth-Udden Scale [Wentworth, 1922]. Table 2 shows the actual diameters in the Φ (phi) notation and their metric equivalent. Particles in the model have a uniform density of 2650 kg m⁻³, corresponding to that of siliciclastic components. According to the Zanke [1982] equations, nonspherical particles are characterized by lower sinking velocities and lower critical velocities for the onset of deposition, suspension and bottom transport. Thus they tend to be easier to be transported and more difficult to be deposited than spherical particles. For the sake of straightforwardness we have varied only particle sizes in this study and refer to the concept of equivalent (Stokes) diameters to take into account particles with differing density and/or shape.

[25] Particle sources in the model are idealized point sources which are located at the model surface and bottom (see Figure 2b). Since the absolute sedimentary mass flux is not addressed by the model calculations, a uniform and wide spectrum of particle sizes (3 to 8 Φ) is released at each of these sources with the commence of and every 6 hours during the upwelling event resulting in 21 particle releases. Particle emission in the model sources does not a priori consider whether the availability of these size classes is likely or not. The actual likeliness of the modeled transport paths is subject of consideration in the discussion section. In addition, the model does not take into account particles located within the water column at the beginning of the experiment.

3. Discussion of Modeling Results

3.1. Hydrodynamic Circulation Patterns

[26] The horizontal velocity field derived from the hydrodynamic calculations is shown in Figure 3, both for the

present day (plots on the left) and with a lower sea level (plots on the right). Presentation in the sigma coordinate system allows for high resolution of the SBL and BBL which both are characterized by intense vertical velocity gradients. In order to simplify the interpretation of the plots grey-scale shading can be used to convert the sigma values into the actual water depth. The following observations primarily apply to the present-day setup, and differences at the lower sea level geometry will be discussed subsequently.

[27] In general, north-directed wind-forcing results in a typical upwelling circulation pattern characterized by an offshore surface current and an onshore bottom current. Figures 3b and 3c illustrate a temporal sequence of successive velocity fields during the early stages of the event, offshore surface velocities rapidly build up, whereas the bottom return flow is still slow and poorly localized. In the following, magnitudes of velocities further rise, especially in the realm of the BBL which, in addition, becomes more and more localized. Maximum velocities at the surface nearly coincide with the point in time when wind-forcing ends (Figure 3b). Offshore velocities up to 0.65 m s⁻¹ culminate within the outer shelf range, whereas bottom onshore currents are most vigorous above the upper shelf (up to 0.30 m s⁻¹) and form an insulated second maximum above the outer shelf break. After cessation of wind drag, surface currents rapidly slow down, whereas the bottom current is more persistent and still present at the end of the model run. In detail, the domain of highest velocities is systematically displaced from the inner shelf to an outer shelf position (as documented in Figure 3c). Summarizing, bottom currents are less closely coupled to the driving mechanism and behave more inertial, especially at the deeper parts of the model profile. Thus the onshore current in the BBL is most vigorous at the inner shelf and just after wind-forcing but more long-lasting at the outer shelf and uppermost slope.

[28] If identical boundary conditions are applied to the model with a lower sea level, the velocity patterns are significantly modified. Maximum offshore velocities now occur at the uppermost slope closely adjacent to the shelf break (i.e., position of the present-day outer shelf break) and their magnitude surpasses the present-day maximum (Figure 3b, 0.7 m s⁻¹). In contrast, maximum bottom velocities are located at the outer shelf break and are somewhat lower (0.25 m s⁻¹) than in the present-day model; a distinct second maximum is situated at the uppermost shelf adjacent to the shore. After the cessation of wind drag relatively large velocities remain observable within the shelf domain (Figure 3c); compared to the present-day pattern, significant bottom currents persist much more proximate to the shore.

[29] Vertical velocities are shown at the end of wind-forcing (after 10 days; Figure 3d). In both cases, the present-day geometry as well as the low sea level setting, maximum velocity values are calculated along steep areas of the continental slope (Figure 3d). Distribution of vertical velocities corresponds to known velocity fields. Unfortunately, neither vertical velocity measurements are available from the Walvis Bay nor data are available for such extreme wind-forcing events from other parts of the world.

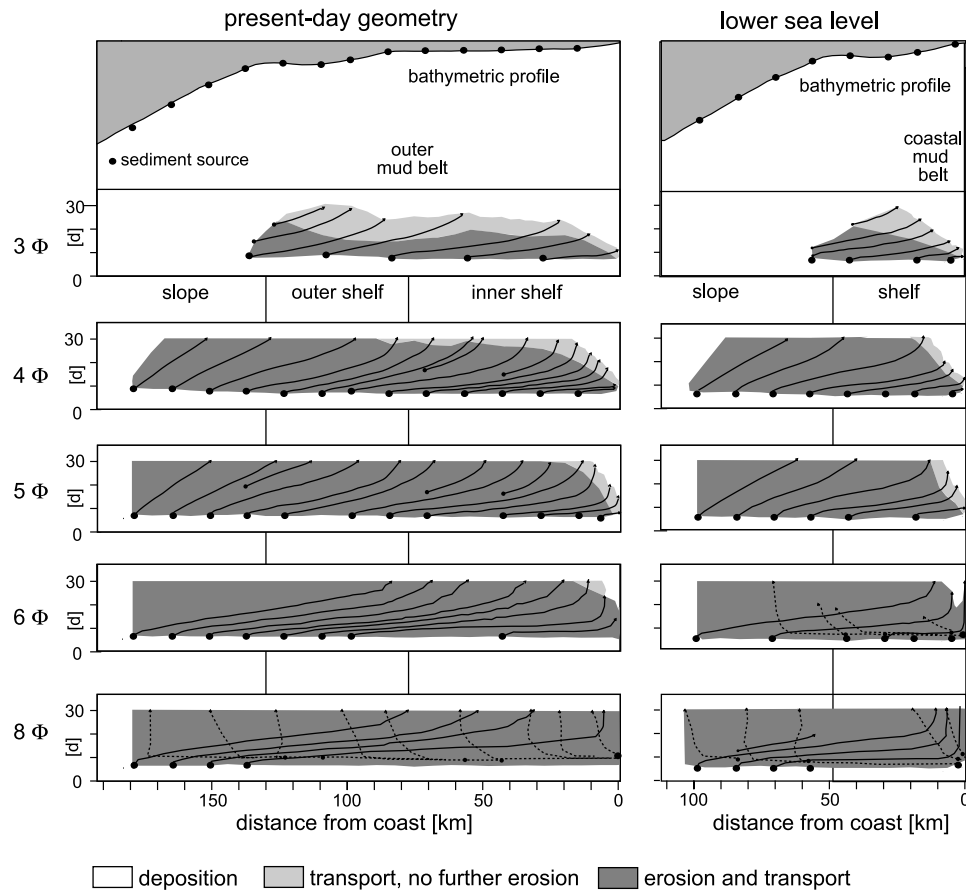


Figure 4. Horizontal displacement of selected bottom-source particles over time; the slope of individual time-displacement paths relates to transport velocity: Gently inclined sections indicate rapid horizontal transport. Solid sections stand for onshore transport, and dashed sections stand for offshore transport; shaded areas mark the occurrence of erosion and transport at the bottom, respectively. The transport of coarse-grained particles is restricted to the shelf domain and to the early stages of the model run; in contrast, smaller particles are transported throughout the model run, especially at the slope. The transport direction of fine-grained particles can be inverted near the coast during early stages of the model run, when particles are lifted into the surface current by upwelling water masses.

[30] Leading over to the particle tracing results, the transport characteristics are controlled by the physical properties of an individual particle (grain size, shape, and density), the location and time of its injection and the hydrodynamic velocity field. Results are time series for individual tracers, including their position and current state (sinking through the water column, deposited, transported within the BBL).

3.2. Particle Transport in the BBL

[31] The occurrence of particle transport within the BBL is illustrated in Figure 4 with respect to particle size, source location and injection time. Again, we first focus on the present-day model (Figure 4, left). Before the onset of wind-forcing (time < 6 days), no bottom-parallel transport is present in the models. In contrast, during the wind-forcing event, onshore-directed bottom currents are capable to erode and transport all particle sizes over the whole model transect, except the fine sand fraction (3Φ) which is only transported within the shelf domain. After the decay of wind-forcing, the current system incrementally slows down, but residual bottom-parallel velocities are still present at the

end of the model run. On the upper slope, almost any particle size fraction, except fine sand and coarse silt particles (3 and 4Φ) keeps in motion; on the shelf, however, velocities decrease more rapidly and particles are deposited all over the shelf (3 and 4Φ), or at least at some parts of the inner shelf (5 and 6Φ). The finest particle fraction (8Φ) is not deposited at any point of the model transect. In the next section, we quote the observed results for individual grain sizes with respect to presence, duration and velocity of transport in the BBL.

[32] The 3Φ particles are eroded on the entire shelf during the upwelling event, whereas particles on the slope are not affected by erosion. Transport on the shelf is relatively short-lived and decays within 5 (in the vicinity of the shore) to 20 days (at the outer shelf domain) after the cessation of wind-forcing. The duration of transport relates roughly to the local water depth; that is, the outer part of the shelf basin remains an area of transport for some days after its cessation on the inner shelf. The 4Φ particles behave significantly different, since during the wind-forcing event they are subject of transport along almost the entire profile

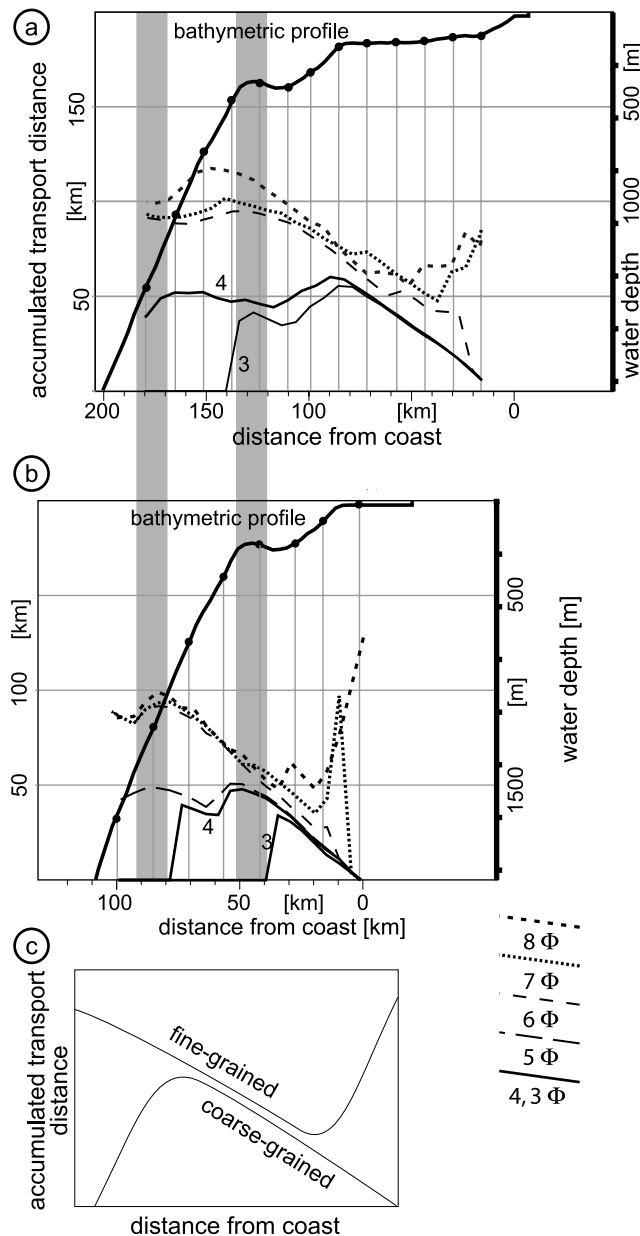


Figure 5. Accumulated transport distances of bottom source tracers released at the beginning of the model run for (a) present-day and (b) lower sea level geometry; sediment types are marked by different line styles (see legend on the right). (c) Simplified trends for transport distances; maxima occur for two groups of fine-grained particles, i.e., particles inserted at the upper slope and those which are released at the shelf and transported back offshore from the coast. Black dots mark positions of sediment sources at the seafloor.

(except for depths of more than about 1400 m). Transport duration surpasses that of sand particles and displacements sum up to larger amounts. An additional maximum in transport duration emerges at the slope and the outer shelf basin, where tracers keep in motion about 20 days.

[33] The mobility of silt-size particles further increases toward smaller grain sizes, allowing for transport at the

upper slope and outer shelf during the whole model run. The 5 and 6 Φ particles are only deposited on the innermost shelf within distinct areas. The 8 Φ particles are in motion virtually anytime and at any position along the model profile. Some 8 Φ particles are lifted into the SBL where they are transported offshore (dashed lines). This effect is only observed at the coast during the wind-forcing event, so that only tracers from bottom sources in the vicinity of the shore are affected.

[34] The lower sea level model with a narrow shelf region (Figure 4, plots on the right) produces some significant differences. Owing to the smaller lateral extent of the shelf, transport of 3 Φ particles is limited to a small belt and does only less expand to the uppermost slope (though it is at the same water depth as the present-day outer shelf). This implies that the preservation potential of coarse sediments on the uppermost shelf is not reduced by a sea level drop. The patterns of 4 Φ and 5 Φ tracer transport resemble the present-day results in terms of maximum transport depth, but the transport duration on the shelf is significantly shorter. Furthermore, deposition areas for these grain sizes are much narrower than under present-day conditions and limited to the innermost part of the shelf. Since these domains are highly energetic owing to wave and tide effects, permanent deposition of particles $\geq 6 \Phi$ is unlikely during low sea level stands; in contrast, under present-day conditions, a mud belt is predicted to occur around the inner shelf break.

[35] The accumulated transport distance of particles released at the beginning of the experiment at the seafloor is plotted against source locations in Figure 5. In general, onshore transport in the BBL is limited by natural barriers (as the shore or steeply dipping sections) so that path lengths tend to decrease toward nearshore sources. This pattern is modified by spatial restrictions for the transport of coarse-grained particles and the occurrence of offshore transport of fine-grained particles. Therefore, dependent on grain size, two diametrically opposed patterns can be recognized. (1) For coarse-grained particles the largest off-sets are monitored for source loci between the inner shelf break and the slope; the smaller the particle diameter is, the more distal the respective source loci are. For source loci more proximate to the shore transport distances monotonously decrease. (2) Fine-grained particles from far offshore slope sources achieve large transport distances. As for larger particles, transport widths incrementally decrease for source loci closer to the shore, but inversion of transport direction and subsequent offshore transport allows for large values next to the shore. In detail, there are significant second-order variations along the profile due to local depth and inclination of the seafloor.

3.3. Transport of Particles From Surface Sources

[36] Tracing of surface-source particles provides transport paths which may consist of multiple sections related to sinking through the water column and transport within the SBL and along the BBL, respectively. In general, residual times of particles in the water column are strongly related to the physical particle properties; analytical sinking distances are listed in Table 2. However, fine-grained material can be affected significantly by the vertical velocity component which may also allow for lifting particles toward higher

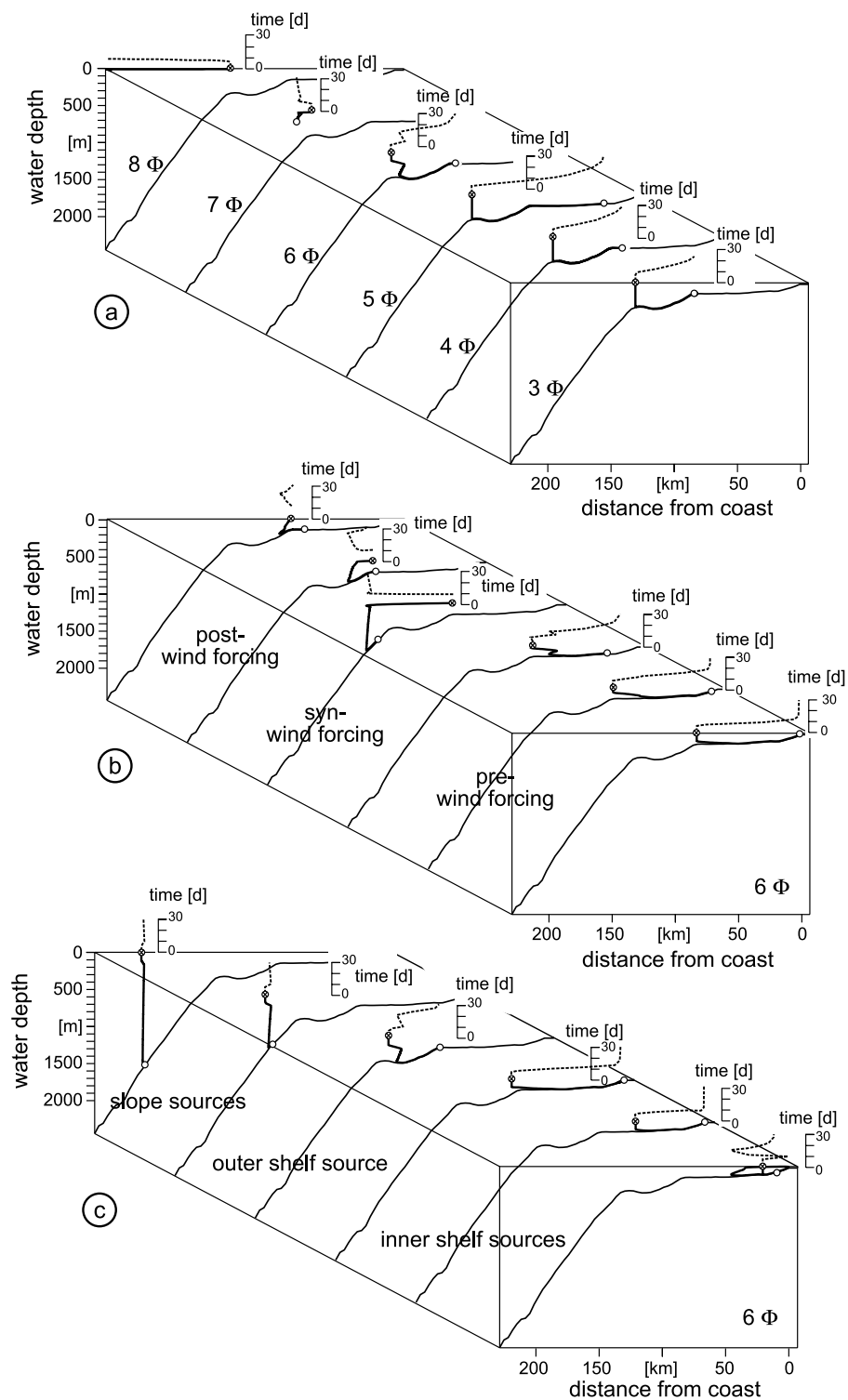


Figure 6. Individual transport paths of surface source tracers. Solid paths are transport in the model plane; dashed paths are horizontal offset versus time; solid circles are source location; open circles are final particle position. (a) Grain-size fractionation of tracers released at the outer shelf break at the beginning of the model run. The net transport is directed offshore for small particle sizes and onshore for larger particles. Maximum transport distances are obtained by two distinct grain-sizes (i.e., $\Phi = 8$ and $\Phi = 5$). (b) Variations due to injection time for grain size $\Phi = 6$ tracers released at an inner shelf break source. The direction of net transport is generally onshore, but turns offshore for tracers released during wind-forcing. (c) Spatial variations along the modeled profile for $\Phi = 6$ tracers injected at the beginning of the model run. Maximum onshore transport occurs at inner shelf sources. Tracers may be subject to onshore-offshore-onshore transport cycles. Sinking paths are most variable at outer shelf source tracers.

water levels. Systematic evaluation of individual transport paths in terms of residual times, predominant transport processes, as well as net transport width and direction leads to general trends reported in the following sections.

3.3.1. Differentiation Due to Particle Sizes

[37] Grain-size fractionation is most striking for early injected tracers from surface sources in the shelf and upper slope areas (Figure 6a). The 8 Φ tracers released at the beginning of the model run are transported more than 150 km offshore during the 5-day wind-forcing event. Since sinking is limited (see Table 2), the material remains in the SBL and can easily reach the open ocean. Deposition of clay and fine silt particles (8 and 7 Φ) is not observed at any locus during the time span covered by the model. Disturbance by repeated upwelling events may prevent deposition of clay-size material permanently, claiming for pellet formation or flocculation processes to explain the presence of natural clay and fine silt deposits.

[38] The $\Phi = 6$ particles travel through the water column within a couple of days to weeks. The respective transport paths obviously monitor variations in the horizontal velocity in different levels of the water column (see the following sections). In general, in the uppermost part, particles may be transported significantly offshore, while the most outstanding landward transport occurs in the lowermost part of the profile. In effect, net horizontal displacement may be directed toward the shore or away from it, depending on the efficiency of transport processes in the BBL. The behavior of $\Phi = 6$ particles will be discussed in detail below.

[39] Summarizing, the net transport is directed offshore for small particle sizes and onshore for larger particles; with opposite direction, maximum transport distances are obtained by two distinct grain sizes, in particular 8 Φ and 5 Φ .

3.3.2. Variations Due to Injection Time

[40] Systematic variations of transport paths are also found to occur owing to the time of particle injection; in general, three different clusters are observed which can be related to pre-, syn-, and post-wind-forcing input of particles. These variations are most prominent at 6 Φ tracers from shelf sources (Figure 6b). Tracers inserted before the onset of wind-forcing sink through the water column without significant lateral offset and are subsequently transported onshore by the evolving bottom current. Depending on the actual injection time and locus, many of these tracers can reach the vicinity of the shore. Maximum offshore transport by the surface current is obtained by tracers inserted during the wind-forcing event. After having passed the surface layer by slow gravitational sinking, horizontal velocities rapidly decrease until the bottom boundary layer of the upper slope domain is reached. There onshore-directed transport is capable to move particles up to the lower shelf, where they are deposited; incremental decrease of the transport velocity results from the general deceleration of upwelling circulation which is, in addition, more pronounced in the shelf domains. The succession of offshore surface transport, sinking and onshore bottom transport results in a net offshore-directed offset for a significant range of injection loci and times. Tracers inserted at later stages of the model run receive only small offshore transport, which occurs, in turn, distributed over an increasing depth range. Since bottom currents are still capable to result

in significant transport distances, net transport direction turns again to onshore transport. However, none of the lately injected 6 Φ tracers is able to overcome the inner shelf break.

3.3.3. Variations Dependent on the Source Position

[41] The variability of transport paths due to different source locations is illustrated for $\Phi = 6$ tracers inserted at the beginning of the model run in Figure 6c. Tracers injected at the surface above the slope undergo a long sinking phase and they are then transported by the onshore bottom current. Since lateral offset during sinking is limited, the net transport direction is onshore; for tracers from less distal sources, transport widths rapidly increase, because travel-times through the water column decrease and bottom currents are more efficient (owing to the shallower water depths and earlier arrival at the bottom). Therefore surface tracers inserted at an upper slope position can easily reach the outer shelf basin. Though particles from outer shelf sources reach the bottom even earlier, time-displacement curves at Figure 6c indicate that bottom currents are less persistent in the shelf domain and onshore transport widths stagnate in this domain.

[42] In contrast, surface tracers inserted at sources between the inner shelf break and the shore rapidly reach the bottom layer where they are subject of efficient onshore transport. All of these tracers reach the shore, implying that maximum transport widths occur at particles inserted at the inner shelf break. Tracers from the innermost shelf are brought back into the surface layer by coastal upwelling and are transported offshore again, so that another cycle of sinking and bottom onshore transport begins. Net transport direction of these tracers may be onshore or offshore, dependent on the actual source position and injection time. Summarizing, two distinct maxima of net transport width are present for 6 Φ tracers, one caused by the longevity of bottom currents in the upper slope domain and one by their elevated velocities in the upper shelf domain.

3.4. Natural Modifications of Model-Predicted Results

[43] A summarizing overview of the particle tracing results with respect to particle grain size is given in Figure 7. Since all grain sizes considered in the models are listed, the actual occurrence of the respective particles and particles paths in natural upwelling systems may be a matter of debate. However, on one hand, this is a general parameter sensitivity study which should include all sediment types. On the other hand, bearing in mind the in situ production of bioclasts, the concept of equivalent diameters and the large scale of the model, virtually any particle size might be available at any source locus, and the topic is more appropriately addressed in terms of relative abundance or likelihood of transport paths. In detail, the character of bottom sources may vary on small scales owing to the local lithofacies; in contrast, distal surface sources are generally short of coarse material, while particle sizes $\geq 5 \Phi$ may be abundant owing to eolian input. The transport path variations presented in Figures 6b and 6c (6 Φ) clearly obeys this condition.

[44] The modeling results imply that a distinct short-lived wind-forcing event results in long-standing upwelling circulation, which remains capable to transport sedimentary particles at least 20 days after its cessation. However,

grain size		Φ	prevailing transport process (over time)	net horizontal transport direction	inversion of transport direction
sand	3	4	bottom-parallel transport bottom tr.	onshore	
	5				
silt	6	7	depends on time/ location	depends on time/ location	abundant
	8		sinking and advection in water column	offshore	
clay					

Figure 7. Comprehensive summary of the observed grain-size-dependent temporal and spatial transport limits, transport directions, and prevailing processes of bottom released tracers.

natural wind-forcing conditions are far more complex, involving gradual variations in wind amplitudes and directions as well as recurrence of upwelling events within time intervals which are much smaller than the modeled time span [e.g., *Hay and Brock, 1992; Shannon and Nelson, 1996; Hagen et al., 2001*]. Thus particles in nature may be even more mobile than those in the model. This is especially true for the shallow water domains, where modeled bottom currents rapidly cease in the absence of wind-forcing. Tides and waves may modify the transport behavior in these regions. Hence, to investigate the sediment transport pattern along the Benguela upwelling systems, particularly the central Namibia upwelling cell off Walvis Bay, we have to simulate a sequence of wind events [e.g., *Shannon and Nelson, 1996*]. However, most effects and trends in sediment transport occur during the wind-forcing as well as the next 5 days straight afterward.

[45] In addition, while the presented 2D modeling results should be quite insensitive to the effect of the coast-parallel (i.e., out-of-plane) Benguela Current, an inversely directed undercurrent (as proposed by *Barange and Pillar [1992]* and *Giraudeau et al. [2000]*) could result in an offshore-directed background bottom current, a scenario which can only be tested within a 3D model. Under those conditions, the deeper parts of the modeled section might be controlled rather by this undercurrent than by surface wind-forcing and the predicted onshore transport across the shelf break would be limited. The actual sphere of influence of the potent upwelling currents proposed by the models may be various over time and dependent on local oceanographic factors.

Hence superimposition of ocean currents and upwelling offers a broad field for further numerical investigations.

4. Conclusions

[46] The impact of an individual short-lived wind-driven upwelling event on transport of sedimentary particles has been modeled using a 2D finite difference circulation model and a Lagrangian particle tracing technique. In order to evaluate the effect of this particular process, the influence of ocean currents, tides and other processes has been factored out.

[47] Under these circumstances, sediment transport by upwelling circulation has been found to remain present even 20 days after the cessation of wind-forcing whereas most processes occur during the wind-forcing itself as well as immediately during the next 5 days afterward as also expected from nature. Thereby, onshore currents within the BBL persist significantly longer than offshore currents in the SBL. In detail, BBL currents are most vigorous during wind-forcing at the shelf but more long-lived at the upper slope.

[48] In terms of consequent particle transport, motion of coarse-grained particles is restricted to the shelf domain and to the early stages of the model run. In contrast, smaller particles are transported throughout the model run, especially at the slope. The transport direction of fine-grained particles released at the bottom can be inverted near the shore during early stages of the model run, when particles are lifted into the SBL by upwelling water masses. On the basis of these results a more precise interpretation of sediment core data with a large age offset caused by the

different redistribution process of foraminifera and alkenones will be possible.

[49] The most complex variations of individual transport paths have been observed at tracers released from surface sources. Variations are most prominent for silt particles early released within the shelf domain, where the polarity of net transport may change owing to grain size, injection time, and source locus.

[50] A lowered sea level modifies the transport capabilities by means of the bathymetric offset and resulting changes in the circulation pattern. Coarse sediments are only transported within the narrowed shelf domain. Thus the preservation potential of upper slope deposits is not affected. In contrast, the presence of mud belts on the shelf, which is in good agreement with the present-day model results, is unlikely under low sea level conditions. This result correlates with field observations which presume a seaward migration of the sediment deposition center during the LGM along the continental coastline off Namibia [e.g., Mollenhauer et al., 2002].

[51] The presented combination of Eulerian and Lagrangian modeling techniques has proved their capability to point out general patterns of marine particle transport. Future work is planned to cover enhancements in terms of a wider range of particle physics as well as more complex hydrodynamic settings using a 3D approach. On one hand, dissolution processes or aggregate formation/breakage could be handled by the model via temporally variable particle sizes and shapes. On other hand, superimposition of ocean currents and upwelling offers a broad field for further numerical investigations.

[52] **Acknowledgments.** This study was funded by the Deutsche Forschungsgemeinschaft via the Research Center Ocean Margins whose financial support is gratefully acknowledged. C. Schäfer-Neth is thanked for fruitful discussions and practical help concerning the ROMS models. This is RCOM publication RCOM0494.

References

- Allen, J. R. L. (1985), *Principles of Physical Sedimentology*, 272 pp., Allen and Unwin, London.
- Bang, N. D. (1971), Southern Benguela Current region in February, 1966, 2. Bathymetry and air-sea interactions, *Deep Sea Res.*, 18(2), 209–224.
- Barange, M., and S. C. Pillar (1992), Cross-shelf circulation, maintenance and dispersal of the euphausiids *Euphausia hanseni* and *Nyctiphanes capensis* in the northern Benguela upwelling system, *Cont. Shelf Res.*, 12, 1027–1042.
- Bremner, J. M. (1983), Biogenic sediments on the South West African (Namibian) continental margin, in *Coastal Upwelling: Its Sedimentary Record. Part B: Sedimentary Records of Ancient Coastal Upwelling*, edited by J. Thiede and E. Suess, pp. 73–103, Plenum, New York.
- Chamley, H. (1990), *Sedimentology*, 285 pp., Springer, New York.
- Chapman, P., and L. V. Shannon (1985), The Benguela ecosystem 2. Chemistry and related processes, in *Oceanography and Marine Biology: An Annual Review*, vol. 23, edited by M. Barnes, pp. 183–251, Aberdeen Univ. Press, Aberdeen, U. K.
- Christensen, B. A., and J. Giraudeau (2002), Neogene and Quaternary evolution of the Benguela coastal upwelling system, *Mar. Geol.*, 180, 1–270.
- de Vries, P., and K. Döös (2001), Calculating Lagrangian trajectories using time-dependent velocity fields, *J. Atmos. Oceanic Technol.*, 18, 1092–1101.
- Ezer, T., H. G. Arango, and A. F. Shchepetkin (2002), Developments in terrain-following ocean models: Intercomparisons of numerical aspects, *Ocean Modell.*, 4, 249–267.
- Garzoli, S. L., A. L. Gordon, V. Kamenkovich, D. Pillsbury, and C. Ducombe-Rae (1996), Variability and sources of the south eastern Atlantic circulation, *J. Mar. Res.*, 54, 1039–1071.
- Gibbs, R. J. (1985), Estuarine flocs: Their size, settling velocity, and density, *J. Geophys. Res.*, 90, 3249–3251.
- Giraudeau, J., G. W. Bailey, and C. Pujol (2000), A high-resolution time-series analyses of particle fluxes in the northern Benguela coastal upwelling system; carbonate record of changes in biogenic production and particle transfer processes, *Deep Sea Res., Part II*, 47(9–11), 1999–2028.
- Goharzadeh, A., A. Saidi, D. Wang, W. Merzkirch, and A. Khalili (2005), An experimental investigation of the Brinkman layer thickness at a fluid-porous interface, in *One Hundred Years Boundary Layer Research*, edited by G. E. A. Meier and K. R. Sreenivasan, pp. 445–454, Springer, New York.
- Hagen, E., R. Feistel, J. J. Agerbag, and T. Ohde (2001), Seasonal and interannual changes in Intense Benguela Upwelling (1982–1999), *Oceanol. Acta*, 24(6), 557–568.
- Haidvogel, D. B., and A. Beckmann (1999), *Numerical Ocean Circulation Modeling*, 344 pp., Imperial Coll. Press, London.
- Haidvogel, D. B., H. G. Arango, K. Hedstrom, A. Beckmann, P. Malanotte-Rizzoli, and A. F. Shchepetkin (2000), Model evaluation experiments in the North Atlantic basin: Simulations in nonlinear terrain-following coordinates, *Dyn. Atmos. Oceans*, 32, 239–281.
- Haupt, B. J. (1995), Numerische Modellierung der Sedimentation im nördlichen Nordatlantik, *Ber. Sonderforsch. 313*, 129 pp., Univ. Kiel, Kiel, Germany.
- Haupt, B. J., C. Schäfer-Neth, and K. Statterger (1994), Modeling sediment drifts: A coupled oceanic circulation-sedimentation model of the northern North Atlantic, *Paleoceanography*, 9(6), 897–916.
- Hay, W. W., and J. R. Brock (1992), Temporal variations in intensity of upwelling off southwest Africa, in *Upwelling Systems: Evolution Since the Early Miocene*, Geol. Soc. Spec. Publ., vol. 63, edited by C. P. Summerhayes, W. L. Prell, and K. C. Emeis, pp. 463–497, Geol. Soc., London.
- Hsü, K. J. (1989), *Physical Principles of Sedimentology*, 231 pp., Springer, New York.
- Khalili, A., M. Huettel, and W. Merzkirch (2001), Techniques for fine-scale boundary layer measurements, in *The Benthic Boundary Layer: Transport Processes and Biogeochemistry*, edited by B. P. Boudreau and B. B. Jørgensen, pp. 44–69, Oxford Univ. Press, New York.
- Lass, H. U., M. Schmidt, V. Mohrholz, and G. Rausch (2000), Hydrographic and current measurements in the area of the Angola-Benguela Front, *J. Phys. Oceanogr.*, 30, 2589–2609.
- Luther, M. E., and J. J. O'Brien (1985), A model of the seasonal circulation in the Arabian Sea forced by observed winds, *Prog. Oceanogr.*, 14, 353–385.
- Lutjeharms, J. R. E., and P. L. Stockton (1987), Kinetics of the upwelling front off southern Africa, *S. Afr. J. Mar. Sci.*, 5, 35–49.
- McCave, I. N., and T. F. Gross (1991), In-situ measurements of particle settling velocity in deep sea, *Mar. Geol.*, 99, 403–411.
- Middleton, G. V., and J. B. Southard (1984), *Mechanics of Sediment Movement, Short Course*, vol. 3, 401 pp., Soc. of Econ. Paleontol. and Mineral., Tulsa, Okla.
- Mohrholz, V., M. Schmidt, and J. R. E. Lutjeharms (1999), The hydrography and dynamics of the Angola-Benguela Frontal Zone and environment in April, *S. Afr. J. Sci.*, 97, 199–208.
- Mollenhauer, G., R. R. Schneider, P. J. Müller, V. Spieß, and G. Wefer (2002), Glacial/interglacial variability in the Benguela upwelling system: Spatial distribution and budgets of organic carbon accumulation, *Global Biogeochem. Cycles*, 16(4), 1134, doi:10.1029/2001GB001488.
- Mollenhauer, G., T. I. Eglinton, N. Ohkouchi, R. R. Schneider, P. J. Müller, P. M. Grootes, and J. Rullkötter (2003), Asynchronous alkenone and foraminifera records from the Benguela upwelling system, *Geochim. Cosmochim. Acta*, 67, 2157–2171.
- Nelson, G., and L. Hutchings (1983), The Benguela upwelling area, *Prog. Oceanogr.*, 12, 333–356.
- Penven, P., C. Roy, J. R. E. Lutjeharms, A. Colin de Verdiere, A. Johnson, F. Shillington, P. Freon, and G. Brundrit (2001), A regional hydrodynamic model of the Southern Benguela, *S. Afr. J. Sci.*, 97, 472–476.
- Peterson, R. G., and L. Stramma (1991), Upper-level circulation in the South Atlantic Ocean, *Prog. Oceanogr.*, 26, 1–73.
- Pufahl, P. K., M. A. Maslin, L. D. Anderson, and shipboard scientific party (1998), Lithostratigraphic summary for Leg 175; Angola-Benguela upwelling system, in *Benguela Current; covering Leg 175 of the cruises of the drilling vessel JOIDES Resolution, Las Palmas, Canary Islands, to Cape Town, South Africa, sites 1075–1087, 9 August–8 October, 1997*, edited by L. A. Baez and J. M. Scroggs, *Proc. Ocean Drill. Program Initial Rep.*, 175 (1), 533–542.
- Seidov, D., and B. J. Haupt (1995), Simulated ocean circulation and sediment transport in the North Atlantic during the last glacial maximum and today, *Paleoceanography*, 12, 281–305.

- Shannon, L. V. (1985), The Benguela Ecosystem, I. Evolution of the Benguela, physical features and processes, *Oceanogr. Mar. Biol.*, 23, 105–182.
- Shannon, L. V., and G. Nelson (1996), The Benguela: Large scale features and processes and system variability, in *The South Atlantic: Present and Past Circulation*, edited by G. Wefer et al., pp. 163–210, Springer, Berlin.
- Shannon, L. V., and M. J. O’Toole (1999), Integrated overview of the oceanography and environmental variability of the Benguela current region, *Syn. Assess. Inf. Benguela Current Large Mar. Ecosyst. (BCLME) Thematic Rep. 2*, 58 pp., U. N. Dev. Programme, Windhoek, Namibia.
- Shchepetkin, A. F., and J. C. McWilliams (1998), Quasi-monotone advection schemes based on explicit locally adaptive dissipation, *Mon. Weather Rev.*, 126, 1541–1580.
- Shchepetkin, A. F., and J. C. McWilliams (2004), The Regional Oceanic Modeling System: A split-explicit, free-surface, topography-following-coordinate ocean model, *Ocean Modell.*, 9, 347–404.
- She, J., and J. M. Klinck (2000), Flow near submarine canyons driven by constant winds, *J. Geophys. Res.*, 105, 28,671–28,694.
- Smith, S. D. (1988), Coefficients for sea surface wind stress, heat flux, and wind profiles as a function of wind speed and temperature, *J. Geophys. Res.*, 93, 15,467–15,472.
- Smith, W. H., and D. T. Sandwell (1997), Global sea floor topography from satellite altimetry and ship depth soundings, *Science*, 277(5334), 1956–1962.
- Song, Y. T., and D. B. Haidvogel (1994), A semi-implicit ocean circulation model using a generalized topography-following coordinate system, *J. Comput. Phys.*, 115, 228–244.
- Song, Y. T., and D. Wright (1998), A general pressure gradient formulation for ocean models. Part II: Energy, momentum, and bottom torque consistency, *Mon. Weather Rev.*, 126, 3231–3247.
- Stander, G. H. (1964), The Benguela Current off south west Africa, *Invest. Rep. Mar. Res. Lab. S. W. Afr.*, 12(43), 5–81.
- Thurman, H. V., and A. P. Trujillo (1999), *Essentials of Oceanography*, 527 pp., Prentice-Hall, Upper Saddle River, N. J.
- Wedepohl, P. M., J. R. E. Lutjeharms, and J. M. Meeuwis (2000), Surface drift in the south-east Atlantic Ocean, *S. Afr. J. Mar. Sci.*, 22, 71–79.
- Wefer, G., et al. (1996), Late Quaternary surface circulation of the South Atlantic: The stable isotope record and implications for heat transport and productivity, in *The South Atlantic: Present and Past Circulation*, edited by G. Wefer et al., pp. 461–502, Springer, Berlin.
- Wentworth, C. R. (1922), A scale of grade and class terms for clastic sediments, *J. Geol.*, 30, 377–392.
- Zabel, M., A. Ahke, F. Aspetsberger, and shipboard scientific party (2003), Report and preliminary results of Meteor-cruise M 57/2 Walvis Bay—Walvis Bay, 11.2.-12.3.2003, *Ber. Fachbereich Geowissenschaften Univ. Bremen*, vol. 220, pp. 1–136, Univ. Bremen, Bremen, Germany.
- Zanke, U. (1982), *Grundlagen der Sedimentbewegung*, 402 pp., Springer, Berlin.

K. Huhn, A. Paul, and M. Seyferth, DFG Research Center Ocean Margins, P.O. Box 330440, D-28334 Bremen, Germany. (khuhn@uni-bremen.de)